


Regular-Orbit-Engineered Chaotic Photon Transport in Mixed Phase Space

Li-Kun Chen,¹ Yu-Zhong Gu,¹ Qi-Tao Cao,¹ Qihuang Gong,^{1,2,3,4} Jan Wiersig,⁵ and Yun-Feng Xiao^{1,2,3,4,*}¹State Key Laboratory for Artificial Microstructure and Mesoscopic Physics, School of Physics, Peking University, Beijing 100871, China²Frontiers Science Center for Nano-optoelectronics & Collaborative Innovation Center of Quantum Matter, Beijing 100871, China³Collaborative Innovation Center of Extreme Optics, Shanxi University, Taiyuan 030006, China⁴Beijing Academy of Quantum Information Sciences, Beijing 100193, China⁵Institut für Physik, Otto-von-Guericke-Universität Magdeburg, Postfach 4120, D-39016 Magdeburg, Germany (Received 27 February 2019; revised manuscript received 20 August 2019; published 24 October 2019)

The dynamical evolution of light in asymmetric microcavities is of primary interest for broadband optical coupling and enhanced light-matter interaction. Here, we propose and demonstrate that the chaos-assisted photon transport can be engineered by regular periodic orbits in the momentum-position phase space of an asymmetric microcavity. Remarkably, light at different initial states experiences different evolution pathways, following either regular-chaotic channels or pure chaotic channels. Experimentally, we develop a nanofiber technique to accurately control the excitation position of light in the phase space. We find that the coupling to high- Q whispering gallery modes depends strongly on excitation in islands or chaotic sea, showing a good agreement with the theoretical prediction. The engineered chaotic photon transport has potential in light manipulation, broadband photonic devices, and phase-space reconstruction.

DOI: 10.1103/PhysRevLett.123.173903

Optical microcavities, storing energies in small volumes for a long time, have served as a crucial platform for light-matter interactions in both fundamental and applied physics [1,2]. Boundary perturbations and deformations have been introduced to microcavities as a universal approach to manipulate light and study wave chaos [3–5]. Over the past years, novel phenomena have been investigated, such as dynamical tunneling [6–8], non-Hermitian physics [9,10], and optical chirality [11–13]. The study on deformed microcavities has also triggered versatile applications including directional light emission [14–20], enhanced photon storage [21,22], nanoparticle detection [23,24], and low-coherence lasers [25,26]. Recently, evolution of light within a cavity has not only attracted abundant interest in mode interaction [27,28], quality factor (Q) spoiling [14,29,30], and turnstile transport [31,32], but also elevated the efficiency and bandwidth of optical coupling [33–36].

For a general deformed microcavity, the position-momentum phase space is mixed with both chaotic and regular regions [37]. The regular orbits such as island chains provide new possibilities for investigating rich chaotic dynamics and manipulating photon evolution [38–43]. In this Letter, we study the chaos-assisted photon transport in the mixed phase space of an asymmetric microcavity, which can be engineered by regular periodic orbits centered in islands. The evolution of light inside the cavity is sensitive to its excitation position in phase space, which is accurately controlled by a nanofiber. Experimentally, the coupling efficiency to the high- Q whispering-gallery modes (WGMs) is investigated, and it is found that the light excited in islands is inhibited

dramatically from tunneling into WGMs. Figure 1(a) shows a cavity-waveguide coupling system, where the deformed “face” cavity with one single symmetric axis has a deformation around 4% [34,44]. The material of the cavity and the

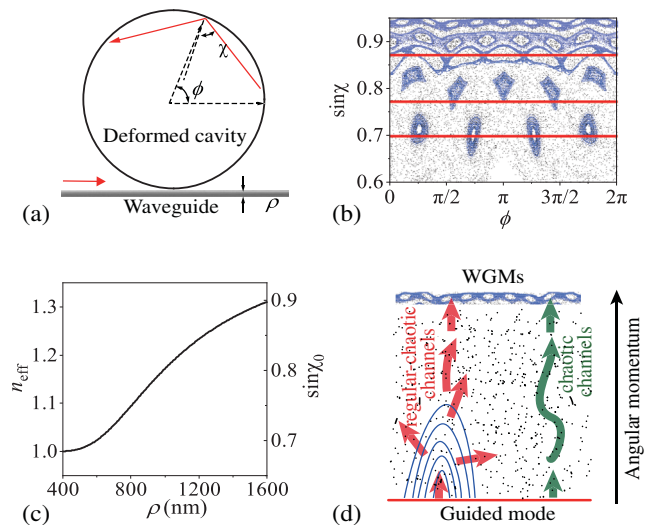


FIG. 1. (a) Schematic diagram of a deformed cavity coupled to a nanofiber waveguide. The internal ray dynamics is depicted using incident angle χ and polar angle ϕ . (b) The Poincaré surface of the section for ray dynamics. The red lines mark the excitation positions of light for various diameters ρ of the nanofiber. From top to bottom, $\rho = 1350$ nm, 890 nm, and 540 nm. (c) The effective index n_{eff} of the waveguide mode at the telecom band and its corresponding initial angular momentum $\sin\chi_0$. (d) Schematics of the photon transport along different paths.

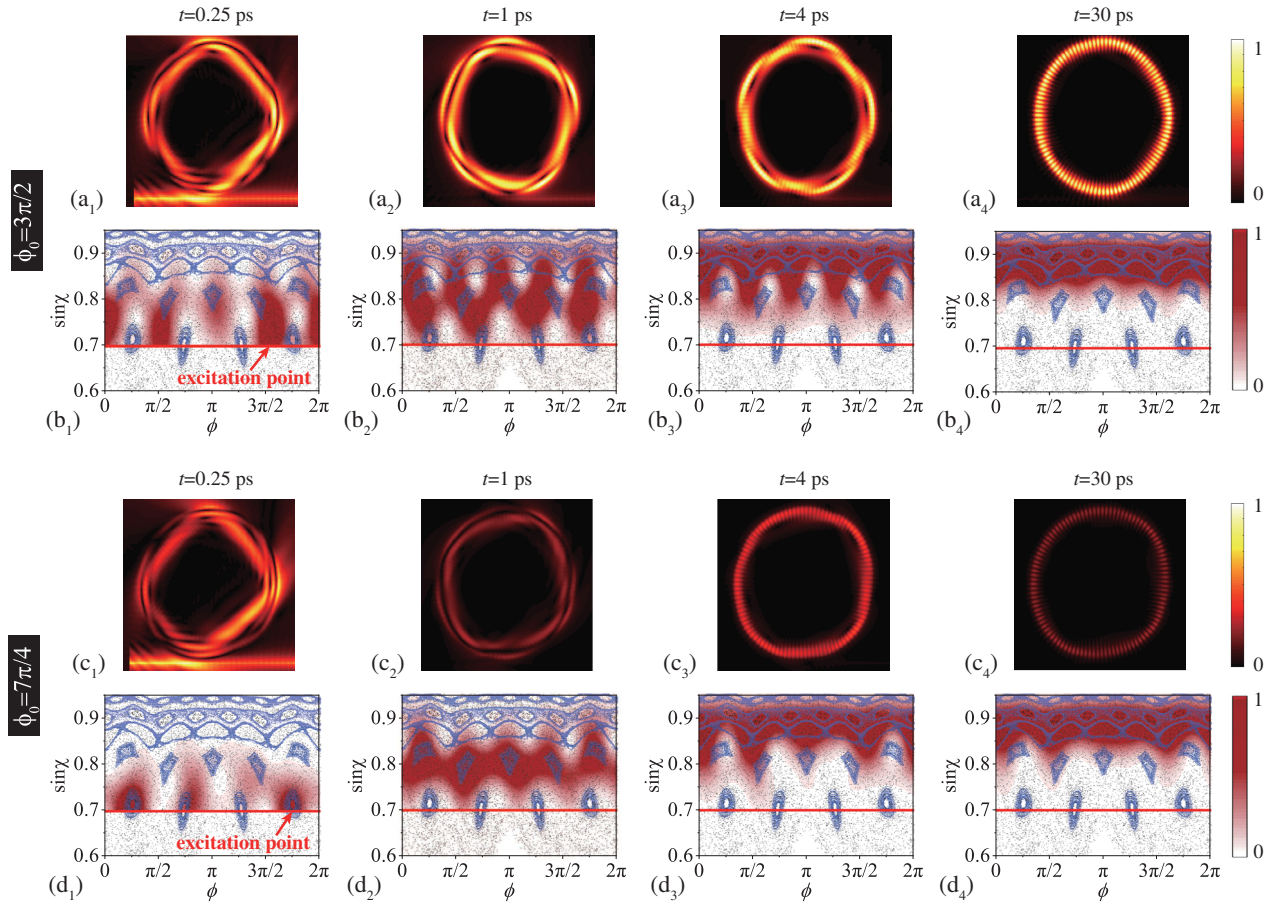


FIG. 2. Short-time snapshots of the 3D FDTD simulation of field distribution at the microcavity plane and its Husimi projection. A 10-fs duration pulse is coupled into the microdisk with a diameter of $20 \mu\text{m}$, through a 540-nm-diameter waveguide. The initial angular momentum of light is marked as a red line in the Husimi projection. Upper and bottom panels: Light excited in chaotic sea and islands, with $\phi_0 = 3\pi/2$ and $7\pi/4$, respectively. (a₁)–(d₁) Light being refracted into the chaotic sea (island chain) at $t = 0.25$ ps. (a₂)–(d₂) Chaotic motion of light at $t = 1$ ps. (a₃)–(d₃) Dynamic tunneling of light into a WGM at $t = 4$ ps. (a₄)–(d₄) The established WGM at $t = 30$ ps. The field intensities in (c₃) and (c₄) are amplified by 5 for better visibility.

nanofiber waveguide is silica, with a refractive index of 1.45. The photon transport in the deformed cavity can be studied by employing the ray model in the Poincaré surface of the section [37] spanned by polar angle ϕ and (dimensionless) angular momentum $\sin \chi$, with χ being the incident angle of the light rays. The critical angle χ_c for internal reflection satisfies $\sin \chi_c \approx 0.69$. Note that here both the Goos-Hänchen shift and the Fresnel filtering correction [45–47] are considered in ray dynamics [48]. As shown in Fig. 1(b), the phase space is mixed, containing chaotic motions (black dots) in the chaotic sea and regular motions (blue orbits) on Kolmogorov-Arnold-Moser (KAM) tori [37] and in island chains. These different structures in phase space are classically disjointed in the ray model, while they can couple together in the wave regime by dynamical tunneling.

In this Letter, we develop a technique to precisely control the excitation position in phase space by intentionally varying the effective mode index n_{eff} and angular position ϕ of the coupled waveguide. Figure 1(c) plots the effective mode index depending on the fiber diameter ρ .

Thus, according to Snell’s law, n_{eff} can be mapped to the initial angular momentum $\sin \chi_0$ of light plotted at the right vertical axis. The waveguide modes and WGMs can be bridged by chaotic photon transport in an asymmetric cavity [34]. Two distinct pathways of light evolution emerge: (i) Light excited in the chaotic sea is transported along the chaotic channels, and it eventually tunnels to WGMs localized on the KAM tori; (ii) light excited in islands first tunnels to the chaotic sea and, second, is transported there along chaotic channels and ultimately tunnels to WGMs; cf. Fig. 1(d).

The dynamics of the light evolution is investigated by full three-dimensional finite-difference time-domain (3D FDTD) simulations. The temporal distribution of the field intensity is shown in Figs. 2(a₁)–2(a₄) and 2(c₁)–2(c₄) at some typical moments. The field distribution is then used to perform Husimi projection in the phase space [49], shown in red in Figs. 2(b₁)–2(b₄) and 2(d₁)–2(d₄). When light is injected in the chaotic sea, it directly enters into the chaotic channels, as confirmed by the intracavity field and its

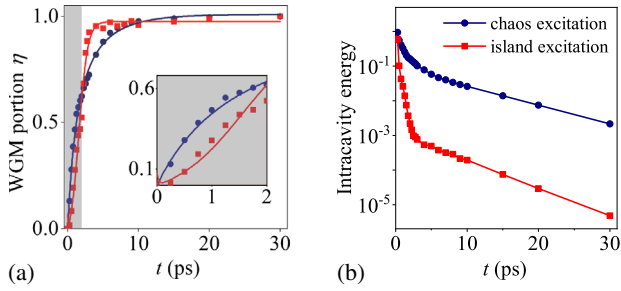


FIG. 3. (a) Temporal evolution of the excited WGM portion η , derived from spatial intensity distribution (dots) and theoretical fitting (curves). Inset: Zoom-in of the first 2 ps. (b) Temporal intracavity energy normalized to the injection energy in the waveguide.

Husimi projection at $t = 0.25$ ps in Figs. 2(a_i) and 2(b_i). Then, the light experiences swift transport in phase space to approach KAM tori from 0.25 ps to 1 ps and finally dynamically tunnels into WGMs. When light is excited in the four-period island chain, however, it generally establishes the island mode first as confirmed by Figs. 2(c₁) and 2(d₁). Then, the light dynamically tunnels from island to chaotic sea from 0.25 ps to 1 ps, along with a dramatic loss of energy. The successive evolution is similar to the chaotic sea case.

To quantitatively explore the evolution process, the WGM proportion η is calculated as the projection of the short-time electrical field to the established WGM. As shown in Fig. 3(a), the WGM portion in the first 2 ps for light excited in the chaotic sea (blue dots) grows more rapidly than that in islands (red dots), but vice versa after 2 ps. Such conclusions can also be confirmed by the vertical distributions of Husimi projection in Figs. 2(b₂) and 2(d₂) (before 2 ps) and Figs. 2(b₃) and 2(d₃) (after 2 ps). We further calculate the intracavity energy of the electric field at each moment as shown in Fig. 3(b). We find that the island case endures a remarkable energy loss, especially in the first 2 ps due to the low- Q characteristics of the island mode. As a result, the final intensity of the established WGM excited in the chaotic sea is 2 orders of magnitude stronger than that excited in the islands. Meanwhile, the coupling efficiency of this WGM excited in the chaotic sea is much higher than that of the islands extracted from the transmission spectra in the fiber. This result supports the fact that the coupling rates from the guided mode to WGM can be engineered by the islands.

The evolution processes above can be modeled by a two-level system and a three-level system for excitation in the chaotic sea and islands, respectively. By treating the transitions incoherently [50], equations of motion for the chaos excitation are given by

$$\frac{dn_m}{dt} = -\gamma_m n_m + g_1(n_c - n_m), \quad (1a)$$

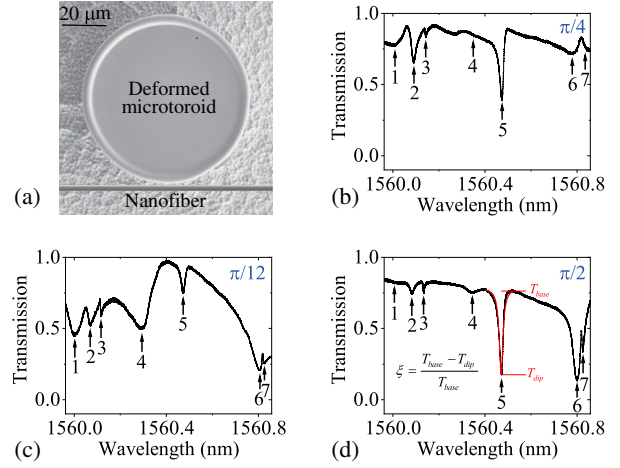


FIG. 4. (a) Scanning electron microscope image of a deformed microtoroid coupled to a nanofiber. The principal (minor) diameter of the cavity is $80 \mu\text{m}$ ($5 \mu\text{m}$), and the thickness of the disk part is $2 \mu\text{m}$. (b)–(d) Typical transmission spectra at the coupling positions $\phi_0 = \pi/12, \pi/4, \pi/2$, showing a Q factor of about 5×10^6 . The diameter of the waveguide is 890 nm . The coupling efficiency ξ is acquired by $(T_{\text{base}} - T_{\text{dip}})/T_{\text{base}}$.

$$\frac{dn_c}{dt} = -\gamma_c n_c + g_1(n_m - n_c), \quad (1b)$$

and equations for the island excitation are

$$\frac{dn_m}{dt} = -\gamma_m n_m + g_1(n_c - n_m), \quad (2a)$$

$$\frac{dn_c}{dt} = -\gamma_c n_c + g_1(n_m - n_c) + g_2(n_i - n_c), \quad (2b)$$

$$\frac{dn_i}{dt} = -\gamma_i n_i + g_2(n_c - n_i). \quad (2c)$$

Here, n_m , n_c , and n_i are the photon numbers in the WGM, chaotic, and islands fields with decay rates γ_m , γ_c , and γ_i . Note that g_1 (g_2) is the tunneling coefficient between the chaotic region and the WGM region (island). Because of the large separation between the island region and the WGMs in phase space, it is reasonable to neglect the direct tunneling between these two regions. From Eqs. (1) and (2), the WGM proportion $\eta = n_m/(n_m + n_c)$ (two-level system) and $\eta = n_m/(n_m + n_c + n_i)$ (three-level system) are analytically obtained and used to fit the simulation data in Fig. 3(a). In practice, the simulation data for island excitation are well fitted only by the three-level system but not a two-level system, which supports the necessity of considering the islands. Moreover, the fitting results show that $\gamma_i \gg \gamma_c > \gamma_m$ and $g_1 \approx g_2$, which is in accordance with the theoretical model of island excitation.

Experimentally, a silica microtoroid with the atomic smoothness surface is adopted to achieve ultrahigh- Q WGMs for mode statistics on the transmission spectra (Fig. 4) [51]. Here, it is noted that the flat disk-torus interface could lead to a potential barrier, while its effect is

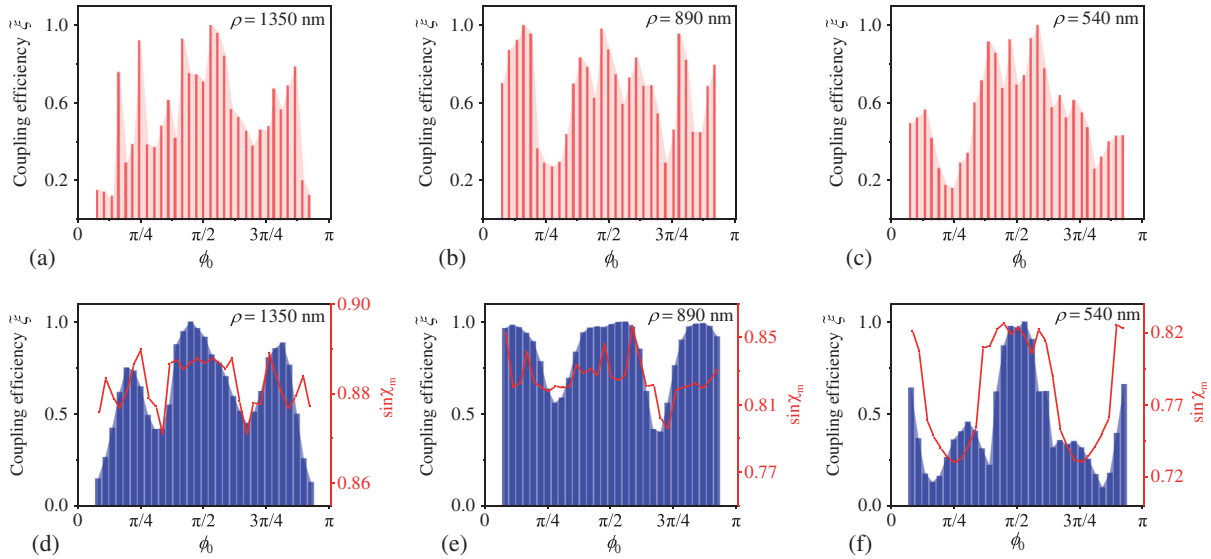


FIG. 5. (a)–(c) Experimental coupling efficiencies ξ of target WGMs depending on the excitation position ϕ_0 with different fiber diameters. (d)–(f) Coupling efficiencies of target WGMs in 3D FDTD simulation (left axis, blue histogram) and mean values of $\sin\chi_m$ (right axis, red curve) in the ray model. Microtoroid geometry for simulation: principal (minor) diameter $44\ \mu\text{m}$ ($4\ \mu\text{m}$).

quite weak under our condition and thus can be neglected. Three typical fibers with diameters of 540 nm, 890 nm, and 1350 nm are used to excite the microcavity. These diameters correspond to the initial angular momentum of light $\sin\chi_0 = 0.70, 0.77$, and 0.87 , marked as red lines in Fig. 1(b), which cross the four-period, five-period, and six-period island chains in the phase space. The microcavity is mounted on a motorized rotation to obtain the transmission spectra depending on the coupling polar angle ϕ_0 . The transmission spectra are obtained through a continuous-wave input with a transverse magnetic (TM) polarization at the telecom band. Figure 4 shows part of the transmission spectra at different ϕ_0 . Here, WGMs are identified by high Q factors ($> 10^5$, mode 5), while island or chaotic modes are identified by relatively low Q factors ($< 10^3$, mode 4). Moreover, the WGMs claim quite uniform values of the free spectrum range, characteristically larger than that of island or chaotic modes. It is also noted that some of the WGMs appear in a Fano line shape (mode 7) due to the interference with low- Q chaotic modes [50].

We count those WGMs with Lorentzian line shapes and perform statistics on their coupling efficiencies characterized by the depth of the dips in Fig. 4(d). Precisely, we average the coupling efficiencies for all high- Q WGMs at each ϕ_0 to reveal collective behaviors of evolution. In this experiment, the gap between the microcavity and coupled fiber is adjusted to ensure that the target mode coupling is deepest at each ϕ_0 . Figures 5(a)–5(c) show the statistical results of the averaged coupling efficiencies ξ depending on ϕ_0 , with $\sin\chi_0 = 0.70, 0.77$, and 0.87 . It is noted that ξ is normalized by the maximum value of each case of $\sin\chi_0$ for a better comparison between simulation and experimental results.

To understand the experimental results, we gather the coupling efficiencies in the 3D FDTD simulation and acquire the maximum incident angle $\sin\chi_m$ in ray dynamics. In the numerical simulation, the coupling efficiencies are derived from the transmission spectra. Then, we count those WGMs that comply with the criteria noted above, and the statistics on coupling efficiencies are shown in the blue histograms of Figs. 5(d)–5(f). In the ray simulation, we run 500 ray trajectories whose initial conditions are set at each experimental condition of $\sin\chi_0$ and ϕ_0 with small fluctuations in phase space, which are 0.01 and 2° , respectively, estimated by wave simulation. Then, we record the maximum angular momentum they can reach during the evolution process as $\sin\chi_m$, and the statistical mean values are shown as red curves in Figs. 5(d)–5(f). It is expected that the maximum angular momentum of light reaching in ray dynamics reflects the coupling rate to WGMs.

Figure 5 demonstrates that the experimental results of coupling efficiencies varying with ϕ_0 are in agreement with the numerical results and also meet the estimation by ray dynamics. Quantitatively, the correlation functions exceed 0.9 for all three nanofiber conditions between experiment and simulation results. It appears that the coupling efficiencies are high when light is excited in the chaotic sea, while they sharply decrease when light is excited in the island chains. Combining the tunneling mechanism revealed in Fig. 2, it is explicit that light evolution is engineered by its excitation point in phase space.

In summary, we have demonstrated that chaotic photon transport can be engineered by the regular orbits in the mixed phase space of a high- Q asymmetric microcavity. An effective nanofiber technique to probe phase space is developed by accurately controlling the excitation position

of the light. The efficiencies of coupling to high- Q WGMs are found to be distinguishable depending on different photon transport paths. The chaos-assisted photon transport may pave the way for the precise manipulation of light in microcavities.

This project is supported by the National Key R&D Program of China (Grants No. 2018YFB2200401 and No. 2016YFA0301302) and the NSFC (Grants No. 11825402, No. 11654003, No. 61435001, and No. 11527901), and the High-Performance Computing Platform of Peking University.

*yfxiao@pku.edu.cn

<http://www.phy.pku.edu.cn/~yfxiao/>

- [1] K. J. Vahala, *Nature (London)* **424**, 839 (2003).
- [2] A. B. Matsko and V. S. Ilchenko, *IEEE J. Sel. Top. Quantum Electron.* **12**, 3 (2006).
- [3] T. Harayama and S. Shinohara, *Laser Photonics Rev.* **5**, 247 (2011).
- [4] H. Cao and J. Wiersig, *Rev. Mod. Phys.* **87**, 61 (2015).
- [5] X.-F. Jiang, C.-L. Zou, L. Wang, Q. Gong, and Y.-F. Xiao, *Laser Photonics Rev.* **10**, 40 (2016).
- [6] G. Hackenbroich and J. U. Nöckel, *Europhys. Lett.* **39**, 371 (1997).
- [7] S. Shinohara, T. Harayama, T. Fukushima, M. Hentschel, T. Sasaki, and E. E. Narimanov, *Phys. Rev. Lett.* **104**, 163902 (2010).
- [8] B. Dietz, T. Guhr, B. Gutkin, M. Miski-Oglu, and A. Richter, *Phys. Rev. E* **90**, 022903 (2014).
- [9] J. Wiersig, *Phys. Rev. Lett.* **112**, 203901 (2014).
- [10] W. Chen, Ş. K. Özdemir, G. Zhao, J. Wiersig, and L. Yang, *Nature (London)* **548**, 192 (2017).
- [11] J. Wiersig, S. W. Kim, and M. Hentschel, *Phys. Rev. A* **78**, 053809 (2008).
- [12] R. Sarma, L. Ge, J. Wiersig, and H. Cao, *Phys. Rev. Lett.* **114**, 053903 (2015).
- [13] S. Liu, J. Wiersig, W. Sun, Y. Fan, L. Ge, J. Yang, S. Xiao, Q. Song, and H. Cao, *Laser Photonics Rev.* **12**, 1870045 (2018).
- [14] J. Nöckel, A. Stone, and R. Chang, *Opt. Lett.* **19**, 1693 (1994).
- [15] C. Gmachl, F. Capasso, E. Narimanov, J. U. Nöckel, A. D. Stone, J. Faist, D. L. Sivco, and A. Y. Cho, *Science* **280**, 1556 (1998).
- [16] H. G. Schwefel, N. B. Rex, H. E. Tureci, R. K. Chang, A. D. Stone, T. Ben-Messaoud, and J. Zyss, *J. Opt. Soc. Am. B* **21**, 923 (2004).
- [17] J. Wiersig and M. Hentschel, *Phys. Rev. Lett.* **100**, 033901 (2008).
- [18] X.-F. Jiang, Y.-F. Xiao, C.-L. Zou, L. He, C.-H. Dong, B.-B. Li, Y. Li, F.-W. Sun, L. Yang, and Q. Gong, *Adv. Mater.* **24**, OP260 (2012).
- [19] F. Albert, C. Hopfmann, A. Eberspächer, F. Arnold, M. Emmerling, C. Schneider, S. Höfling, A. Forchel, M. Kamp, J. Wiersig, and S. Reitzenstein, *Appl. Phys. Lett.* **101**, 021116 (2012).
- [20] T. Harayama, S. Sunada, and S. Shinohara, *Photonics Res.* **5**, B39 (2017).
- [21] V. Fiore, Y. Yang, M. C. Kuzyk, R. Barbour, L. Tian, and H. Wang, *Phys. Rev. Lett.* **107**, 133601 (2011).
- [22] C. Liu, A. Di Falco, D. Molinari, Y. Khan, B. S. Ooi, T. F. Krauss, and A. Fratalocchi, *Nat. Photonics* **7**, 473 (2013).
- [23] L. Shao, X.-F. Jiang, X.-C. Yu, B.-B. Li, W. R. Clements, F. Vollmer, W. Wang, Y.-F. Xiao, and Q. Gong, *Adv. Mater.* **25**, 5616 (2013).
- [24] N. Zhang, Z. Gu, S. Liu, Y. Wang, S. Wang, Z. Duan, W. Sun, Y.-F. Xiao, S. Xiao, and Q. Song, *Optica* **4**, 1151 (2017).
- [25] B. Redding, A. Cerjan, X. Huang, M. L. Lee, A. D. Stone, M. A. Choma, and H. Cao, *Proc. Natl. Acad. Sci. U.S.A.* **112**, 1304 (2015).
- [26] S. Bittner, S. Guazzotti, Y. Zeng, X. Hu, H. Yilmaz, K. Kim, S. S. Oh, Q. J. Wang, O. Hess, and H. Cao, *Science* **361**, 1225 (2018).
- [27] J. Wiersig and M. Hentschel, *Phys. Rev. A* **73**, 031802(R) (2006).
- [28] C.-H. Yi, H.-H. Yu, and C.-M. Kim, *Phys. Rev. E* **93**, 012201 (2016).
- [29] A. Bäcker, R. Ketzmerick, S. Löck, J. Wiersig, and M. Hentschel, *Phys. Rev. A* **79**, 063804 (2009).
- [30] J. Kullig and J. Wiersig, *Phys. Rev. E* **94**, 022202 (2016).
- [31] S.-B. Lee, J. Yang, S. Moon, S.-Y. Lee, J.-B. Shim, S. W. Kim, J.-H. Lee, and K. An, *Phys. Rev. Lett.* **103**, 134101 (2009).
- [32] J.-B. Shim, S.-B. Lee, S. W. Kim, S.-Y. Lee, J. Yang, S. Moon, J.-H. Lee, and K. An, *Phys. Rev. Lett.* **100**, 174102 (2008).
- [33] J. Yang, S.-B. Lee, S. Moon, S.-Y. Lee, S. W. Kim, Truong Thi Anh Dao, J.-H. Lee, and K. An, *Phys. Rev. Lett.* **104**, 243601 (2010).
- [34] X. Jiang, L. Shao, S.-X. Zhang, X. Yi, J. Wiersig, L. Wang, Q. Gong, M. Lončar, L. Yang, and Y.-F. Xiao, *Science* **358**, 344 (2017).
- [35] L. Wang, C. Wang, J. Wang, F. Bo, M. Zhang, Q. Gong, M. Lončar, and Y.-F. Xiao, *Opt. Lett.* **43**, 2917 (2018).
- [36] Q. Song, *Sci. China Phys. Mech. Astron.* **62**, 074231 (2019).
- [37] A. J. Lichtenberg and M. A. Leiberman, *Regular and Stochastic Motion* (Springer, Berlin, 1983).
- [38] J. U. Nöckel, A. D. Stone, G. Chen, H. L. Grossman, and R. K. Chang, *Opt. Lett.* **21**, 1609 (1996).
- [39] S. Lacey, H. Wang, D. H. Foster, and J. U. Nöckel, *Phys. Rev. Lett.* **91**, 033902 (2003).
- [40] T. Tanaka, M. Hentschel, T. Fukushima, and T. Harayama, *Phys. Rev. Lett.* **98**, 033902 (2007).
- [41] Q. Song, L. Ge, B. Redding, and H. Cao, *Phys. Rev. Lett.* **108**, 243902 (2012).
- [42] H. Kwak, Y. Shin, S. Moon, S.-B. Lee, J. Yang, and K. An, *Sci. Rep.* **5**, 9010 (2015).
- [43] S. Gehler, S. Löck, S. Shinohara, A. Bäcker, R. Ketzmerick, U. Kuhl, and H.-J. Stöckmann, *Phys. Rev. Lett.* **115**, 104101 (2015).
- [44] C.-L. Zou, F.-W. Sun, C.-H. Dong, F.-J. Shu, X.-W. Wu, J.-M. Cui, Y. Yang, Z.-F. Han, and G.-C. Guo, *IEEE J. Sel. Top. Quantum Electron.* **19**, 1 (2012).
- [45] J. Unterhinninghofen, J. Wiersig, and M. Hentschel, *Phys. Rev. E* **78**, 016201 (2008).

- [46] E. G. Altmann, G. Del Magno, and M. Hentschel, *Europhys. Lett.* **84**, 10008 (2008).
- [47] P. Stockschröder, J. Kreismann, and M. Hentschel, *Europhys. Lett.* **107**, 64001 (2014).
- [48] The wave number used in the calculation is $k_0R = 37.82$, and the standard deviation of the Gaussian wave packet is $\sigma = 4$.
- [49] M. Hentschel, H. Schomerus, and R. Schubert, *Europhys. Lett.* **62**, 636 (2003).
- [50] Q.-F. Yang, X.-F. Jiang, Y.-L. Cui, L. Shao, and Y.-F. Xiao, *Phys. Rev. A* **88**, 023810 (2013).
- [51] L. Wang, D. Lippolis, Z.-Y. Li, X.-F. Jiang, Q. Gong, and Y.-F. Xiao, *Phys. Rev. E* **93**, 040201(R) (2016).